Ultraviolet relaxation dynamics of aniline, N, N-dimethylaniline and 3,5-dimethylaniline at 250 nm

Thompson, James O. F.; Saalbach, Lisa; Crane, Stuart W.; Paterson, Martin J; Townsend, David

Published in:
Journal of Chemical Physics

DOI:
10.1063/1.4914330

Publication date:
2015

AIP | The Journal of Chemical Physics

Ultraviolet relaxation dynamics of aniline, N, N-dimethylaniline and 3,5-dimethylaniline at 250 nm

James O. F. Thompson, Lisa Saalbach, Stuart W. Crane, Martin J. Paterson, and Dave Townsend

Citation: The Journal of Chemical Physics **142**, 114309 (2015); doi: 10.1063/1.4914330
View online: http://dx.doi.org/10.1063/1.4914330
View Table of Contents: http://scitation.aip.org/content/aip/journal/jcp/142/11?ver=pdfcov
Published by the AIP Publishing

Ultraviolet relaxation dynamics of aniline, *N*,*N*-dimethylaniline and 3,5-dimethylaniline at 250 nm

James O. F. Thompson,[1] Lisa Saalbach,[1] Stuart W. Crane,[1] Martin J. Paterson,[2] and Dave Townsend[1,2,a)]

[1]*Institute of Photonics and Quantum Sciences, Heriot-Watt University, Edinburgh EH14 4AS, United Kingdom*
[2]*Institute of Chemical Sciences, Heriot-Watt University, Edinburgh EH14 4AS, United Kingdom*

(Received 4 February 2015; accepted 25 February 2015; published online 18 March 2015)

Time-resolved photoelectron imaging was used to investigate the electronic relaxation dynamics of gas-phase aniline, *N*,*N*-dimethylaniline, and 3,5-dimethylaniline following ultraviolet excitation at 250 nm. Our analysis was supported by *ab initio* coupled-cluster calculations evaluating excited state energies and (in aniline) the evolution of a range of excited state physical properties as a function of N–H bond extension. Due to a lack of consistency between several earlier studies undertaken in aniline, the specific aim of this present work was to gain new insight into the previously proposed non-adiabatic coupling interaction between the two lowest lying singlet excited states $S_1(\pi\pi^*)$ and $S_2(3s/\pi\sigma^*)$. The methyl-substituted systems *N*,*N*-dimethylaniline and 3,5-dimethylaniline were included in order to obtain more detailed dynamical information about the key internal molecular coordinates that drive the $S_1(\pi\pi^*)/S_2(3s/\pi\sigma^*)$ coupling mechanism. Our findings suggest that in all three systems, both electronic states are directly populated during the initial excitation, with the $S_2(3s/\pi\sigma^*)$ state then potentially decaying via either direct dissociation along the N–X stretching coordinate (X = H or CH_3) or internal conversion to the $S_1(\pi\pi^*)$ state. In aniline and *N*,*N*-dimethylaniline, both pathways most likely compete in the depletion of $S_2(3s/\pi\sigma^*)$ state population. However, in 3,5-dimethylaniline, only the direct dissociation mechanism appears to be active. This is rationalized in terms of changes in the relative rates of the two decay pathways upon methylation of the aromatic ring system. © *2015 AIP Publishing LLC.* [http://dx.doi.org/10.1063/1.4914330]

I. INTRODUCTION

We have previously reported the results of a time-resolved photoelectron imaging (TRPEI) study of gas-phase aniline using selected excitation wavelengths in the narrow spectral region between 273 and 266 nm.[1] This region is of particular interest as it spans the energetic onset threshold for excitation to the S_2 electronic state.[2] This state exhibits predominantly 3s Rydberg character in the Franck-Condon (FC) region, evolving into more $\pi\sigma^*$ valence character at extended N–H bond distances.[3] Typically, we will therefore use the label $S_2(3s/\pi\sigma^*)$ to reflect this. In a wide range of small molecular systems, including phenols, pyrroles, purines, imidazoles, and indoles, low-lying excited electronic states formed via Rydberg/valence interactions (often simply labelled "$\pi\sigma^*$" states even though they are formally of mixed character) are now thought to be a common feature in the excited state photochemistry. Interest in developing a detailed understanding of the role, such states' play in the electronic relaxation dynamics of these systems is strongly motivated by the fact that they often form the chromophore sites for ultraviolet (UV) absorption in larger biological species. These include, for example, the DNA bases, the melanin pigmentation system, various amino acids, and phenylpropanoids in plants.[4,5] There is growing evidence that non-adiabatic couplings between the electronic and vibrational degrees of freedom in these biological systems may be mediated by mixed Rydberg/valence states, providing a highly efficient route for the dissipation of excess energy into the surrounding environment. This may then reduce the possibility of other potentially more harmful photochemical processes taking place.[5,6] As such, this imparts a critical photostability that may have provided an important evolutionary factor in the development of early life $\sim 3.5 \times 10^9$ years ago—particularly since at that time, the surface of the Earth was subject to much more intense UV irradiation than today as the atmosphere was not yet fully developed.[7] Recent reviews by Ashfold and co-workers[8] and Roberts and Stavros[9] provide excellent overviews of progress made in the study of non-adiabatic interactions involving mixed Rydberg/valence states in a wide variety of systems over the last decade or so.

In addition to the general interest in photostability outlined above, our previous study was also specifically motivated by the fact that investigations undertaken by several other groups had failed to produce a consistent picture of the relaxation dynamics of aniline in the region close to the $S_2(3s/\pi\sigma^*)$ origin. In contrast to many systems, where the $3s/\pi\sigma^*$ state potential energy surface is purely dissociative along the N–H stretching coordinate (e.g., pyrrole, phenol, imidazole), in aniline, it exhibits a shallow well that supports several vibrational levels.[2] This was reflected in the series

a)Author to whom correspondence should be addressed. Electronic mail: D.Townsend@hw.ac.uk

of carefully selected excitation wavelengths chosen for our earlier investigation. Dynamical information was extracted using a global exponential fitting procedure (as outlined here in Sec. II C), yielding a series of energy-resolved decay associated spectra (DAS) reflecting the evolution of electronic and vibrational population from the initially excited aniline molecule on several different time scales. Additional mechanistic insight was also obtained from the photoelectron angular distributions (PADs) provided by the highly differential imaging approach. Our data provided no clear evidence of any non-adiabatic coupling between the $S_2(3s/\pi\sigma^*)$ state and the lower-lying $S_1(\pi\pi^*)$ valance state following excitation in the 273-266 nm region. This appeared to be in general agreement with the findings of several previous time- and frequency-resolved dynamical studies (that employed a range of different experimental approaches and associated observables)[10–12] but at odds with an earlier TRPEI measurement.[13]

At more energetic aniline excitation wavelengths (~250 nm), there is also a lack of consistency between several previously reported studies. Here, the excitation still samples only the $S_1(\pi\pi^*)$ and $S_2(3s/\pi\sigma^*)$ states but deposits more energy into the internal molecular coordinates. Work by Ashfold and co-workers[10] and Stavros and co-workers[12] concluded that excitation in this region leads to non-adiabatic decay of the initially populated $S_1(\pi\pi^*)$ state via rapid internal conversion through a conical intersection (CI) to the $S_2(3s/\pi\sigma^*)$ state. In turn, this then dissociates via N–H bond fission. In the Ashfold study, which employed H atom Rydberg tagging, evidence of the $S_1(\pi\pi^*)/S_2(3s/\pi\sigma^*)$ coupling interaction was inferred from structured features in the H atom kinetic energy release distribution that may be correlated with specific vibrational population within the anilino co-fragment. On the basis of this data, out-of-plane distortions of the aromatic ring system were suggested as a critical CI coordinate. In the Stavros study, time-resolved H atom imaging was supported by high-level complete active space self-consistent field (CASSCF) calculations. The onset of high-kinetic energy H atoms with a rapid appearance time (<1 ps) following 250 nm excitation was taken as an evidence of $S_1(\pi\pi^*) \rightarrow S_2(3s/\pi\sigma^*)$ internal conversion. Time-resolved ion-yield measurements by Longarte and co-workers[11] also support the involvement of an $S_1(\pi\pi^*)/S_2(3s/\pi\sigma^*)$ interaction in aniline following excitation at the same wavelength, although the direction of population transfer between the two states could not be unambiguously determined. Finally, TRPEI work by Fielding and co-workers concluded that excitation at 250 nm is exclusively to the S_2 state, with both the 3s and $\pi\sigma^*$ components being populated simultaneously.[13] These two components were observed to exhibit $1/e$ lifetimes of 200 fs and 1.6 ps, respectively, with the former being attributed to decay via non-adiabatic coupling to the $S_1(\pi\pi^*)$ state (i.e., the reverse of the mechanism proposed by the Ashfold and Stavros groups) and the latter to dissociation along the N–H coordinate (and/or internal conversion to the S_0 ground state at extended N–H distances). This assertion also appears to be supported by recent theoretical calculations.[14]

Our own previous TRPEI studies of aniline were restricted by the fact that we did not, at the time, have access to full UV wavelength tunability for both the pump and probe laser beams required for the experiment. It was therefore not possible to undertake "clean" experiments (i.e., measurements free from probe-pump dynamics evolving to negative time delays) using 250 nm excitation in conjunction with single-photon probe ionization (which is desirable as multi-photon schemes can convolute TRPEI data significantly, making data analysis considerably more challenging). However, recent upgrades in our laboratory have removed this limitation. Given the clear discrepancies between the previous studies outlined above, we have therefore revisited the UV excitation dynamics of aniline and conducted new TRPEI measurements using pump excitation at 250 nm in order to further investigate the nature of the $S_1(\pi\pi^*)/S_2(3s/\pi\sigma^*)$ interaction. We have also performed complementary measurements on the related species *N*,*N*-dimethylaniline (*N*,*N*-DMA) and 3,5-dimethylaniline (3,5-DMA), the structures of which are shown in Fig. 1. Since decay pathways for the $S_2(3s/\pi\sigma^*)$ state in aniline are believed to involve motion along the N–H stretching coordinate and deformations of the aromatic ring system,[10,12] selective methylation of these sites has the potential to offer additional mechanistic insight. We have specifically elected to study 3,5-DMA in order to minimise proximity effects altering the NH_2 group geometry with respect to the aromatic ring system. With the exception of two low-resolution UV-visible (UV-VIS) spectra of *N*,*N*-DMA,[15,16] and a single theoretical study of excited state energies employing CASSCF methods on the same system,[17] no other gas-phase spectroscopic or dynamical information relating to low-lying electronically excited states appears to have been previously reported for either methyl-substituted species. However, assisted by preliminary spectroscopic measurements and theoretical calculations undertaken to support our TRPEI data, a clearer picture of the $S_1(\pi\pi^*)/S_2(3s/\pi\sigma^*)$ interaction is revealed in all cases.

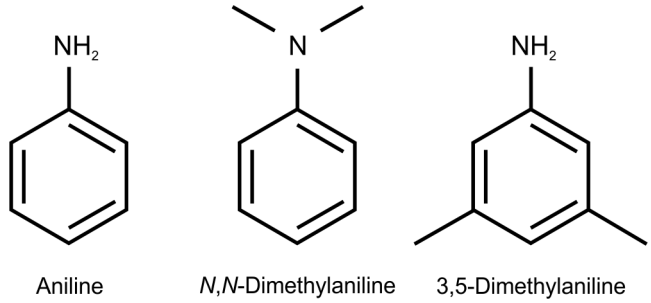

FIG. 1. Schematic representations of aniline, *N*,*N*-DMA, and 3,5-DMA.

II. EXPERIMENTAL

A. Preliminary UV-VIS spectra

Molecular samples used in all aspects of the present study were purchased from Sigma-Aldrich and used without further purification (aniline ≥99.5%, *N*,*N*-DMA 99% and 3,5-DMA 98%). Preliminary room-temperature UV/VIS vapour-phase spectra (see Fig. 2) were recorded for all three molecules using a commercial bench-top spectrophotometer (Shimadzu UV-2550, 0.2 nm scan interval/1 mm slit width). The aniline

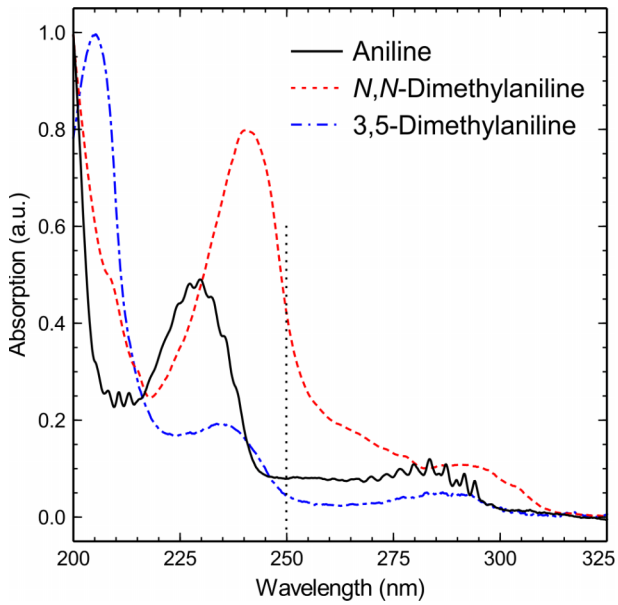

FIG. 2. Preliminary room-temperature UV-VIS spectra obtained for each of the three molecules under study. The vertical dashed line denotes the 250 nm pump energy used in our TRPEI measurements.

data are in excellent agreement with other recently reported measurements.[10,12] The $S_1(\pi\pi^*)$ origin appears at ~294 nm and the region spanning 270-245 nm includes a contribution due to weak excitation to the $S_2(3s/\pi\sigma^*)$ state.[2] At ~240 nm, there is clear onset of strong absorption to a higher-lying state, assigned as having singlet $\pi\pi^*$ character.[12,14,18,19] However, we note that recent theoretical work by Worth and co-workers suggests the existence of two 3p Rydberg states sitting energetically slightly below this $\pi\pi^*$ state.[20] For the purposes of the discussion outlined here, we will therefore simply use the generalized label S_{3+} to denote any feature (or set of features) lying energetically above $S_2(3s/\pi\sigma^*)$.

The spectrum of 3,5-DMA is very similar to that of aniline, albeit with less observable structure and a small red-shift in the positions of the more energetic features. Of key relevance to this work is that the onset threshold for S_{3+} absorption is only red shifted by ~5 nm and so 250 nm excitation will still only populate the $S_1(\pi\pi^*)$ and/or $S_2(3s/\pi\sigma^*)$ states. It is desirable to avoid direct population of higher-lying states in our TRPEI measurements to keep the study of the $S_1(\pi\pi^*)/S_2(3s/\pi\sigma^*)$ interaction free from additional spectral signatures that may convolute the dynamical interpretation. In this regard, *N*,*N*-DMA is potentially problematic if one wishes to also employ a 250 nm pump since all absorption bands appear significantly more red-shifted than in 3,5-DMA. However, we note that the small shoulder contributing to the red edge of the intense S_{3+} absorption feature (clearly visible in the 260-275 nm region and not present in aniline or 3,5-DMA) is most likely attributable to stronger absorption to the $S_2(3s/\pi\sigma^*)$ state in *N*,*N*-DMA—as suggested by the relative sizes of the calculated $S_1(\pi\pi^*)$ and $S_2(3s/\pi\sigma^*)$ oscillator strengths (see Sec. III, Table I). When compared to aniline, it is also likely that the *N*,*N*-DMA data contain a higher proportion of hot-band features appearing to the red of the true S_{3+} origin(s). This is based on the fact that the lowest frequency ground-state vibrational modes of aniline[10,21] are >200 cm^{-1}, whereas in *N*,*N*-DMA, there are CN and CH_3 torsions predicted to exhibit vibrational frequencies <100 cm^{-1}.[22] To the best of our knowledge, ground state vibrational frequencies

TABLE I. Vertical excitation energies (ΔE), oscillator strengths (f), and dipole moments (μ) obtained at various levels of theory for the three molecules under study. For more details see the main text in Section III.

Aniline		ΔE (eV) (CCSD)[a]	ΔE (eV) (CCSD)[b]	ΔE (eV) CCSDR(3)[a]	f (CCSD)[a]	f (CCSD)[b]	μ (D) (CCSD)[a,c]
S_0[d]		0	0	0	...	...	1.468
S_1 ($1\,^1A''$)	$\pi\pi^*$	4.746	4.754	4.661	0.0235	0.0228	2.277
S_2 ($1\,^1A'$)	$\pi\sigma^*$ (NH)/Ns Ryd	4.913	5.047	4.890	0.0055	0.0057	7.911
S_3 ($2\,^1A'$)	$\pi\sigma^*$ (CH)/Cs Ryd	5.585	5.682	5.558	0.0122	0.0507	6.967
S_4 ($2\,^1A''$)	$\pi\pi^*$/Ryd	5.661	5.782	5.647	0.0001	0.0001	3.882
N,*N*-dimethylaniline							
S_0[d]		0	...	0	...	...	1.911
S_1 ($1\,^1A''$)[e]	$\pi\pi^*$	4.585	...	4.486	0.0406	...	4.201
S_2 ($1\,^1A'$)[e]	$\pi\sigma^*$ (CN)/Ns Ryd	4.550	...	4.539	0.0231	...	3.504
S_3 ($2\,^1A''$)	$\pi\sigma^*$ (CH)/Np Ryd	5.136	...	5.131	0.0007	...	1.063
S_4 ($2\,^1A'$)	$\pi\sigma^*$ (CH)/Cs Ryd	5.173	...	5.163	0.0145	...	4.582
3,5-dimethylaniline							
S_0[d]		0	...	0	...	...	1.176
S_1 ($1\,^1A''$)	$\pi\pi*$/Ryd	4.679	...	4.601	0.0247	...	1.782
S_2 ($1\,^1A'$)	$\pi\sigma^*$ (NH)/Ns Ryd	4.795	...	4.770	0.0034	...	8.478
S_3 ($2\,^1A'$)	$\pi\sigma^*$ (CH)/Ryd	5.489	...	5.456	0.0089	...	6.100
S_4 ($2\,^1A''$)	$\pi\sigma^*$ (CH)/Cp Ryd	5.550	...	5.531	0.0008	...	5.856

[a]aug-cc-pVDZ basis set for response properties.
[b]aug-cc-pVTZ basis set for response properties.
[c]Orbital unrelaxed ground state first order property.
[d]S_0 geometry from B3LYP/6-311G(d,p) in C_s symmetry.
[e]Energy ordering based on CCSDR(3) calculation.

for 3,5-DMA have not been previously reported, but it is reasonable to assume that motions associated with the NH_2 group will be similar in frequency to those seen in aniline (i.e., >200 cm^{-1}). We also note, however, that the infrared spectrum of *m*-xylene (1,3-dimethylbenzene) shows vibrational frequencies of ~100 cm^{-1} associated with torsional motion of the CH_3 groups.[23] Critically within the context of our present work, the jet-cooled molecular beam conditions used in our TRPEI experiments should eliminate any hot-band features present in the room temperature spectra. This is explored in more detail below.

B. Preliminary one-color photoelectron spectra

Our experimental setup has recently been described in detail elsewhere.[24] Samples were introduced into the source chamber of a differentially pumped photoelectron spectrometer via an Even-Lavie pulsed molecular beam valve operating at 1 kHz.[25] Small strips of filter paper were soaked with sample and placed in a cartridge mounted within the valve body, directly behind the exit nozzle (150 μm diameter). Helium (1.5 bars) was used as a carrier gas and the temperature of the pulsed valve was regulated at 45 °C (or 60 °C in the case of 3,5-DMA) using a closed-loop chiller. After passing through a skimmer (1.0 mm), the molecular beam entered the main interaction chamber and was intersected at 90° by a UV pulse (254-240 nm). This light was derived from the fundamental output of a 1 kHz regeneratively amplified Ti:Sapphire laser system (Spectra-Physics, Spitfire Pro/Empower) seeded by a Ti:Sapphire oscillator (Spectra Physics, Tsunami/Millennia Pro). The central wavelength of the amplifier output was set to 800 nm with a 30 nm full-width at half maximum (FWHM) bandwidth. A portion of the 800 nm output was sum-frequency mixed in a thin β-barium borate (BBO) crystal with the signal beam from an optical parametric amplifier (Spectra Physics, OPA-800C), pumped by a separate portion of the 800 nm amplifier output. This produced light in the visible region which was frequency doubled into the UV using a second BBO crystal (producing ~1.2 μJ/pulse) and then focussed into the spectrometer using a 25 cm fused silica lens.

One-color (1 + 1) resonance enhanced multi-photon ionization (REMPI) of the molecular samples took place between the electrodes of a magnetically shielded electrostatic lens setup optimised for velocity-map imaging.[26] A 40 mm MCP/P47 phosphor screen detector was used in conjunction with a CCD camera (640 × 480 pixels) to image the resulting photoelectrons. No additional "on-the-fly" processing was performed during data acquisition. Prior to commencing photoelectron data collection, the spectrometer was switched to ion detection mode and the pulsed valve timing conditions adjusted, when necessary, to ensure no dimers or higher-order clusters were present in the molecular sample beam. Ion time-of-flight information was recorded using a small solid state silicon photomultiplier (AP Technologies, MicroEVB-1 mm board, Micro FM-10035-X18 sensor) externally positioned behind the phosphor screen.

Photoelectron images were recorded for all three sample molecules between 254 and 240 nm (stepping the central UV pulse wavelength in 2 nm intervals, which was also the FWHM bandwidth). A commercial grating spectrometer (Ocean Optics, USB2000+) provided accurate wavelength determination. One-colour multiphoton ionization images of pyrrole were also recorded at 240 nm to provide data for time-of-flight to energy calibration of the spectrometer.[27] Following application of a rapid matrix inversion to the raw image data,[24] a series of (1 + 1) photoelectron spectra may be generated. These are presented in Fig. 3. By comparison

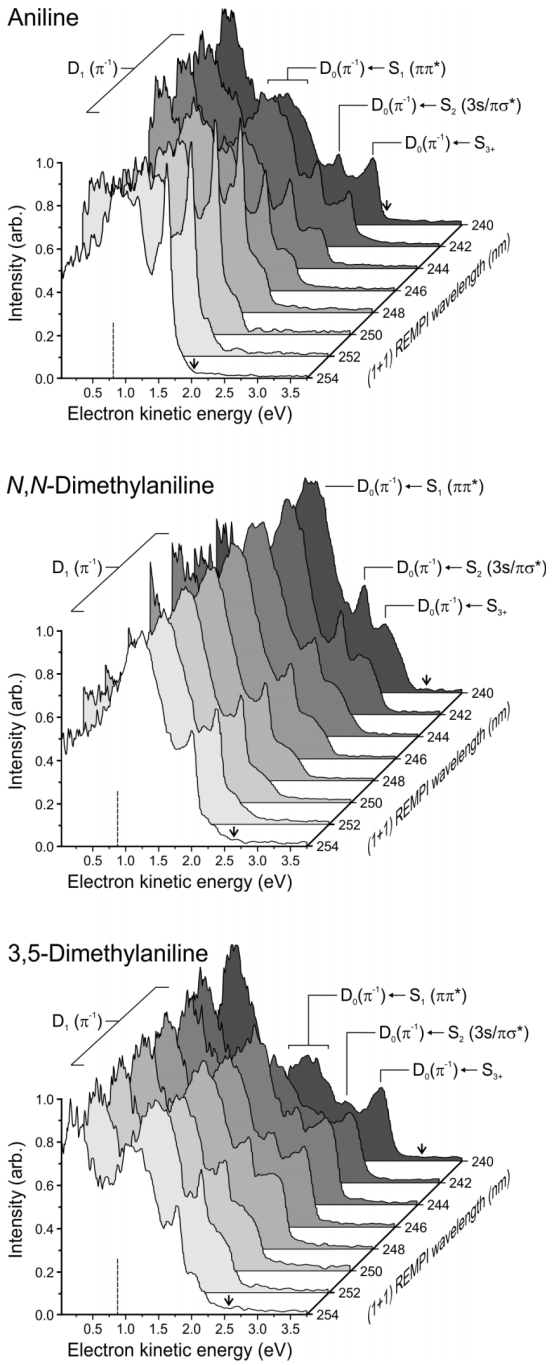

FIG. 3. One-colour (1+1) REMPI spectra of aniline, *N*,*N*-DMA, and 3,5-DMA under molecular beam conditions over excitation energies spanning 250-240 nm. Vertical dashed lines denote the energetic position corresponding to zero kinetic energy in a two-colour (1+1′) REMPI process using a 250 nm pump and 305 nm (aniline) or 310 nm probe. Small vertical arrows indicate predicted maximum photoelectron energy cut-offs based on previously reported adiabatic ionization potentials. For more details, see the main text.

with our previous work in aniline, and also that reported by Fielding and co-workers,[13,28] ionization signals originating from $S_1(\pi\pi^*)$, $S_2(3s/\pi\sigma^*)$, and S_{3+} are labelled on the figure. The adiabatic D_0 (π^{-1}) ionization potentials (IPs) of aniline, *N*,*N*-DMA, and 3,5-DMA are 7.720 eV,[29,30] 7.12 eV,[31,32] and ~7.2 eV,[33] respectively. On the basis of this data, the maximum photoelectron kinetic energy cutoff predicted for aniline is in excellent agreement with that seen in our experimental measurements. In the two methylated species, the agreement is less satisfactory; however, we note that the IPs quoted above for *N*,*N*-DMA and 3,5-DMA are based on band edges of low-resolution He (I) photoelectron spectra, whereas in aniline, the IP was obtained using higher-resolution, laser-based measurements. Using our current data, the position of the high kinetic energy cutoff seen in each of the 8 REMPI spectra obtained for the methylated systems may be used to estimate a revised value for the D_0 (π^{-1}) adiabatic IP. Upon averaging these results, we arrive at 7.26 ± 0.05 eV for *N*,*N*-DMA and 7.48 ± 0.05 eV for 3,5-DMA.

Of specific relevance to the present study is that Fig. 3 clearly shows the onset of excitation to (and ionization from) S_{3+} in all cases—as revealed by the peak appearing on the high kinetic energy edge of the spectra as the wavelength is shortened. In aniline, this feature becomes very pronounced at wavelengths ≤242 nm and appears to have an onset at ~246 nm. At longer wavelengths (≥248 nm), a small shoulder is still evident to the high energy side of the sharp $S_2(3s/\pi\sigma^*)$ feature; however, we believe this is not associated with S_{3+}, as will be expanded upon in more detail later. Both *N*,*N*-DMA and 3,5-DMA exhibit very similar behaviour to that seen in aniline, with the onset of the feature attributable to S_{3+} appearing at ~246-248 nm. We therefore conclude that a 250 nm pump wavelength may be used for TRPEI studies specifically intended to investigate any potential $S_1(\pi\pi^*)/S_2(3s/\pi\sigma^*)$ interaction in all three molecules without inducing any significant excitation to higher-lying states.

Features in the very low kinetic energy region of Fig. 3 most likely correspond to ionization into the D_1 (π^{-1}) cation state. In aniline and *N*,*N*-DMA, these features begin to appear at ~246 nm, whereas in 3,5-DMA, they are present at all REMPI wavelengths investigated. The D_1 (π^{-1}) vertical ionisation potentials (from the ground state) for aniline, *N*,*N*-DMA, and 3,5-DMA are 9.18 eV, 9.00 eV, and 8.55 eV, respectively.[32,33] A (1 + 1) REMPI scheme at 250 nm provides a total energy of 9.92 eV, and so in all spectra presented in Fig. 3, ionization to the D_1 (π^{-1}) cation state is clearly feasible. However, excitation at 250 nm (4.96 eV) is also energetically well above the origins of both the $S_1(\pi\pi^*)$ and $S_2(3s/\pi\sigma^*)$ states (4.22 eV and 4.60 eV, respectively, for aniline).[2,10] As such we may speculate that, on the basis of heuristic Franck-Condon (FC) arguments, the propensity for ionization into the D_1 (π^{-1}) state of the cation is small in these cases. On the other hand, S_{3+} is prepared close to the electronic origin once this threshold for excitation is reached. D_1 (π^{-1}) photoelectron signals may therefore become more pronounced due to more favourable FC overlap—as appears to be observed for the cases of aniline and *N*,*N*-DMA at excitation wavelengths <248 nm. This observation adds additional weight to our assertion that 250 nm excitation induces little or no direct excitation to S_{3+}. In 3,5-DMA, the significantly lower D_1 (π^{-1}) ionization threshold (relative to the two other systems) presumably means that the $S_1(\pi\pi^*)$ and $S_2(3s/\pi\sigma^*)$ states may be ionized efficiently at all one-colour REMPI wavelengths studied.

On the basis of the UV-VIS spectra shown in Fig. 2, pump-probe TRPEI measurements conducted using a probe wavelength >300 nm will ensure that our data are free from any unwanted "probe-pump" dynamical signals due to resonant excitation close to the $S_1(\pi\pi^*)$ origin. For excitation using a 250 nm pump, this gives a combined (pump + probe) photon energy of ~9.0 eV. The vertical dashed lines in Fig. 3 denote energetic positions corresponding to zero photoelectron kinetic energy in such a two-colour (1 + 1′) ionization scheme. It is apparent that, in all cases, only ionization to the D_0 (π^{-1}) cation state is expected to be observed.

C. TRPEI measurements

The general experimental setup was the same as that already described above. In addition to the pump beam (250 nm), a co-propagating UV probe beam (305 nm for aniline or 310 nm otherwise, ~1.8 μJ/pulse) was also now introduced. This was generated by twice frequency doubling the output of a second optical parametric amplifier (Light Conversion, TOPAS Prime-U). The temporal delay between the pump and the probe was precisely controlled using a linear translation stage running under automated computer command. The pump and probe beams were combined on a thin dichroic mirror and focussed into the spectrometer using a 25 cm fused silica lens. To ensure the best possible temporal instrument response function, material dispersion compensation of the pump and probe beams was managed using single-pass fused silica and CaF_2 prism compressors, respectively. By systematically adjusting the length of the prism compressors in each beam line, a pump-probe cross correlation of 130 ± 10 fs was obtained. This was recorded directly inside the spectrometer from non-resonant, two-colour (1 + 1′) multiphoton ionization of pyrrole.[34] Data collection runs repeatedly sampled pump-probe delays of −250 fs to +500 fs in 25 fs increments and +500 fs to +100 ps in a series of 17 exponentially increasing time steps. At each delay position, photoelectron images of the time-invariant one-colour pump alone and probe alone signals were recorded in addition to the pump-probe data for subsequent background subtraction.

Fig. 4 presents representative photoelectron images resulting from (1 + 1′) ionization of aniline, *N*,*N*-DMA, and 3,5-DMA at zero pump-probe delay ($\Delta t = 0$). The left hand half of each image shows the result following application of our rapid matrix inversion approach.[24] Time-resolved photoelectron spectra were generated from the full set of image data recorded for each of the three molecules investigated. These plots are shown in Fig. 5 (note the mixed linear-logarithmic scaling of the time-axis). All data sets show a long-lived feature spanning the low-kinetic energy region up to ~0.7 eV with a weak signal decaying in ~1 ps superimposed on top. A very rapidly decaying feature at energies greater than ~0.6 eV is also evident in all cases. This exhibits a prominent narrow peak on top of a broader, largely unstructured background.

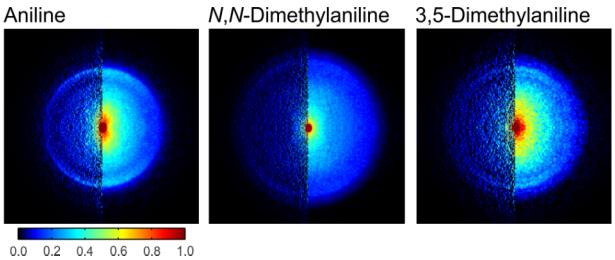

FIG. 4. (1 + 1′) photoelectron images recorded at zero pump-probe delay following excitation at 250 nm and subsequent ionization using 305 nm (aniline) or 310 nm. Time-invariant pump-alone and probe-alone signals have been subtracted and the images are 4-fold symmetrised. The left half of the images show the processed data obtained following application of the matrix inversion method described in Ref. 24. The linear polarization direction of both the pump and probe beams is vertical with respect to the figure.

The time-dependence of the photoelectron data was analysed using a standard Levenberg-Marquardt global fitting routine, wherein the 2D data $S(E, \Delta t)$ are expressed as

$$S(E, \Delta t) = \sum_i A_i(E) \cdot P_i(\Delta t) \otimes g(\Delta t). \quad (1)$$

Here, $A_i(E)$ is the decay associated photoelectron spectrum of the ith data channel, which exhibits a time dependent population $P_i(\Delta t)$ described by a series of exponentially decaying functions (all of which originate from zero pump-probe delay). The experimentally determined Gaussian cross-correlation function is denoted $g(\Delta t)$. This fitting approach yields a series of decay associated spectra (DAS) that plot the relative amplitude of each exponential component as a function of photoelectron kinetic energy. Additional information and some good illustrative examples relating to this approach may be found elsewhere.[35]

In order to non-trivially fit all of the data sets shown in Fig. 5 using Eq. (1), three exponential functions were required. The first, denoted τ_1, decays extremely rapidly, exhibiting a time-constant of ≤100 fs in all cases. The second, τ_2, describes a slightly longer process (550 fs-2.2 ps) while the final function, τ_3, decays on a much more extended time scale (180-230 ps). The numerical lifetimes obtained for aniline are in reasonable agreement with those previously reported.[13] To illustrate the good quality of the overall model, Fig. 5 also shows the corresponding fit and associated residuals for the aniline data. The corresponding DAS plots for each system under study along with the associated time constants (which have ±10% uncertainties) are shown in Fig. 6. Although the shapes and relative amplitudes of the DAS obtained for each system are broadly similar in appearance, a key feature of note is that in aniline and N,N-DMA, the τ_1 DAS exhibits negative amplitude at low kinetic energies, whereas in 3,5-DMA, this is not the case. A similar (although somewhat larger) negative amplitude feature was also observed in DAS data obtained for aniline following 250 nm excitation in the TRPEI work of Fielding and co-workers.[13] The presence of negative amplitude in a given DAS provides a strong indication of sequential dynamical processes. Since all exponentials used in our fit originate from $\Delta t = 0$, any negative amplitude associated with a given DAS describing a short-lived process is effectively compensating for the positive amplitude at short delay times associated with a sequential feature (i.e., one not truly originating from $\Delta t = 0$) described by a second DAS for a longer-lived process in the same energy region. As will be expanded upon further in Sec. IV, the DAS data for 3,5-DMA therefore suggest the relaxation processes occurring may be different in some way to those in aniline and N,N-DMA.

Further dynamical insight may be gained from the temporal evolution of the PADs provided by the imaging approach. As discussed, for example, in reviews by Reid[36] and Suzuki,[37] the time-dependence of the PADs obtained following (1 + 1′) ionization using parallel linear polarizations may be expressed as a function of the photoelectron kinetic energy E and the pump-probe delay time Δt in terms of the well-known anisotropy parameters β_2 and β_4:

$$I(E, \Delta t, \theta) = \frac{\sigma(E, \Delta t)}{4\pi} [1 + \beta_2(E, \Delta t) P_2(\cos\theta) + \beta_4(E, \Delta t) P_4(\cos\theta)]. \quad (2)$$

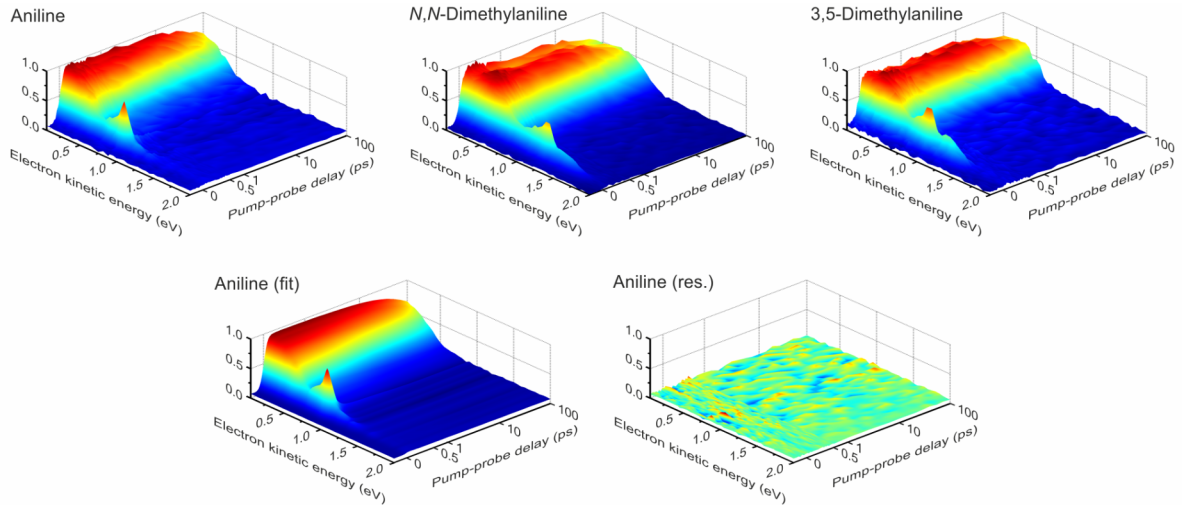

FIG. 5. Time-dependent photoelectron spectra of aniline, N,N-DMA, and 3,5-DMA obtained following excitation at 250 nm with subsequent ionization using 305 nm (aniline) or 310 nm. For clear display of the dynamics over all temporal ranges, the time axis is plotted on a linear scale to +500 fs and logarithmically between +500 fs and +100 ps. The data are partitioned into 0.025 eV energy bins. Also shown is the fit to the aniline data—obtained using the procedure described in the main text—along with the associated residuals (i.e., the fit subtracted from the raw data).

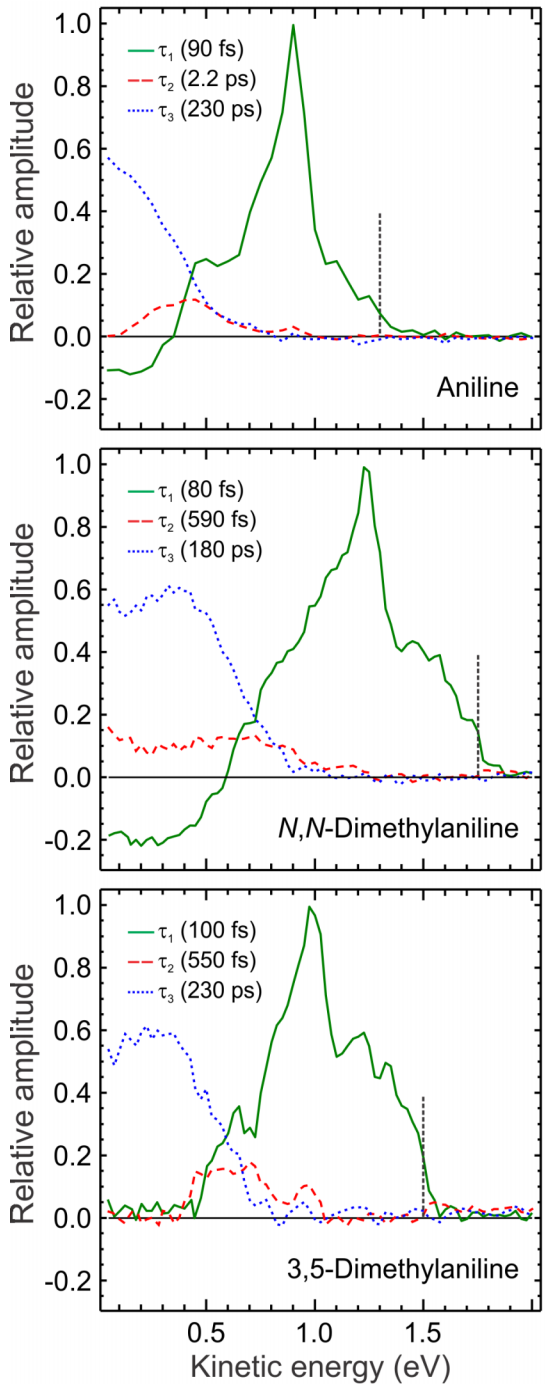

FIG. 6. DAS obtained from a global exponential fit to the data presented in Fig. 5. For additional details, see the main text. The uncertainty in the time constant values is ±10% (one standard deviation) and the data are partitioned into 0.025 eV energy bins. Vertical dashed lines denote predicted maximum photoelectron kinetic energy cut-offs based on the central pump and probe wavelengths and the adiabatic IP. For aniline, a previously determined IP value of 7.72 eV was used. For *N*,*N*-DMA and 3,5-DMA, we used new estimated IP values of 7.26 eV and 7.48 eV, respectively (as discussed in Sec. II B).

Here, the $P_n(\cos\theta)$ terms are the *n*th-order Legendre polynomials, $\sigma(E,\Delta t)$ is the time-dependent photoelectron energy distribution, and $\theta = 180°$ is defined by a vertical line running fully through the images shown in Fig. 4 via the centre point. Fits to our PAD data using Eq. (2) reveal significant time-dependent variation in the β_2 anisotropy parameter for the three systems under study. The β_4 parameters are very small (<±0.05) in all cases and are statistically too noisy to provide any reliable additional information. Fig. 7 plots the temporal evolution of β_2 averaged over broad kinetic energy regions of the photoelectron spectra where long-lived (≥180 ps) signals are observed (as modelled by the τ_3 DAS shown in Fig. 6). In all cases, trends in the temporal variation of β_2 are consistent within these broad energy regions and averaging serves only to improve the statistics in the data presented. Aniline (between 0.05 and 0.50 eV) shows no evidence of any change in β_2 as a function of pump-probe delay. In contrast, *N*,*N*-DMA and 3,5-DMA both exhibit a clear temporal evolution in β_2 over the photoelectron kinetic energy regions spanning 0.05-0.80 eV and 0.05-0.65 eV, respectively. The initial β_2 rise in *N*,*N*-DMA (~200 fs) is considerably shorter than that seen in 3,5-DMA (~1 ps). At higher kinetic energies (i.e., beyond 0.50-0.80 eV, depending on the system), photoelectron signals are extremely short-lived and no information relating to their temporal evolution may be reliably obtained. However, Fig. 7 also shows plots of β_2 vs. photoelectron kinetic energy at zero pump-probe delay superimposed on the corresponding photoelectron spectra. It is immediately apparent that the sharp, intense photoelectron peak seen at ~1 eV in each system has a considerably higher value of β_2 associated with it than other features in the data. This is strongly characteristic of the 3s Rydberg nature of the $S_2(3s/\pi\sigma^*)$ state, as will be expanded upon further shortly.

III. THEORY

Potential energy and property surfaces were obtained using linear response (LR) coupled cluster theory and the related equation of motion (EOM) formalism, in conjunction with an aug-cc-pVDZ basis set. Vertical excitation energies and oscillator strengths (obtained from the linear response transition densities) were evaluated using EOM-coupled cluster with single and doubles (EOM-CCSD) using Gaussian09,[38] while linear response calculations were performed using the Dalton2013 program.[39,40] Equilibrium S_0 geometries were taken from a B3LYP/6-311G(d,p) optimisation in C_s symmetry. At this geometry, the effect of triples was also determined using the non-iterative CCSDR(3) correction to LR-CCSD excitation energies.[41] In all cases, the inclusion of triples lowers the state energies by less than 0.1 eV and gives the first and second excited states as $S_1(\pi\pi^*)$ and $S_2(3s/\pi\sigma^*)$, respectively. However, the two states are almost degenerate in *N*,*N*-DMA and, without the inclusion of triples, the energy ordering of the $\pi\pi^*$ and $3s/\pi\sigma^*$ states is reversed in this system. In the absence of any experimental data confirming the true ordering of these two specific states, we will retain the $S_1(\pi\pi^*)$ and $S_2(3s/\pi\sigma^*)$ labels for all three systems for clarity in subsequent discussions. The data are summarized in Table I. Absolute state energies appear slightly (~0.2 eV) higher than the experimentally observed band maxima seen in the UV-VIS spectra shown in Fig. 2, although overall trends in the relative peak positions appear broadly consistent. Our assignment of the dominant orbital character for the S_3 and S_4 states of aniline is different to that given by Worth and co-workers.[20] We note that these states are heavily

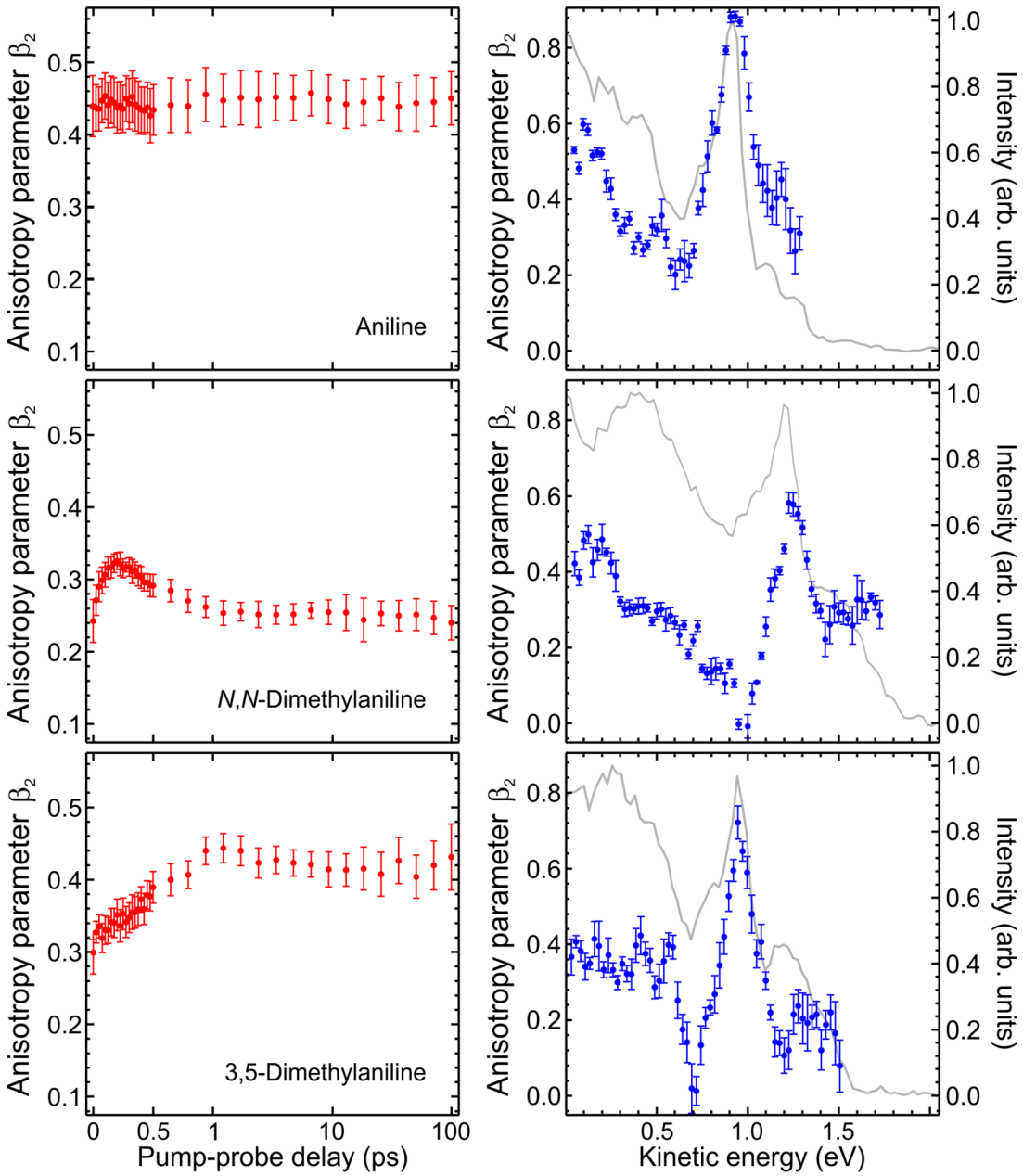

FIG. 7. (Left) anisotropy parameter β_2 as a function of pump-probe delay averaged over a selected range of photoelectron kinetic energies for aniline (0.05–0.50 eV), *N*,*N*-DMA (0.05–0.80 eV), and 3,5-DMA (0.05-0.65 eV) following 250 nm excitation with subsequent 305 nm (aniline) or 310 nm ionization. The time axis is linear to +500 fs and logarithmic between +500 fs and +100 ps. The data were partitioned into 0.025 eV energy bins for initial anisotropy fits (before averaging), and the error bars represent one standard deviation. Fits were performed over the angular region $5° \leq \theta \leq 90°$ to eliminate uncertainties from centre-line noise present in the Abel-inverted images (see Fig. 4). (Right) anisotropy parameter β_2 as a function of photoelectron kinetic energy at zero pump-probe delay (data points) superimposed over the corresponding photoelectron spectrum at zero pump-probe delay (grey line).

mixed, containing contributions from a large number of orbital configurations. Previous assignments were based on EOM-CCSD eigenvectors calculated at the C_{2v} S_0 transition state to NH_2 inversion, whereas our current assignments are made in the same manner but at the C_s S_0 minimum. In all other respects, equivalent calculations presented here and previously yield near identical results.

Rigid scans along the N–H stretching coordinate at the EOM-CCSD level were performed for aniline and 3,5-DMA. Additionally, similar scans were undertaken for both the N–CH_3 and NC–H stretching coordinates in *N*,*N*-DMA (see Fig. 8). In this case, both the $S_1(\pi\pi^*)$ and $S_2(3s/\pi\sigma^*)$ states are strongly bound along NC–H, whereas for N–CH_3, the $S_2(3s/\pi\sigma^*)$ state exhibits only a shallow potential well, analogous to that seen along N–H in the other two systems. For aniline, the evolution of several additional electronic state properties as a function of N–H bond extension was also investigated. Fig. 9(a) plots the normalized EOM-CCSD right eigenvector amplitudes for the orbital transition relating to the $3s/\pi\sigma^*$ state contribution to the S_2 state overall. This falls from 0.70 at 1.01 Å to 0.32 at 1.7 Å. Fig. 9(b) shows the corresponding evolution of the magnitude of the (un-normalized) LCAO coefficient of the uncontracted nitrogen 3s basis function *within* the $3s/\pi\sigma^*$ state (i.e., the N-centered

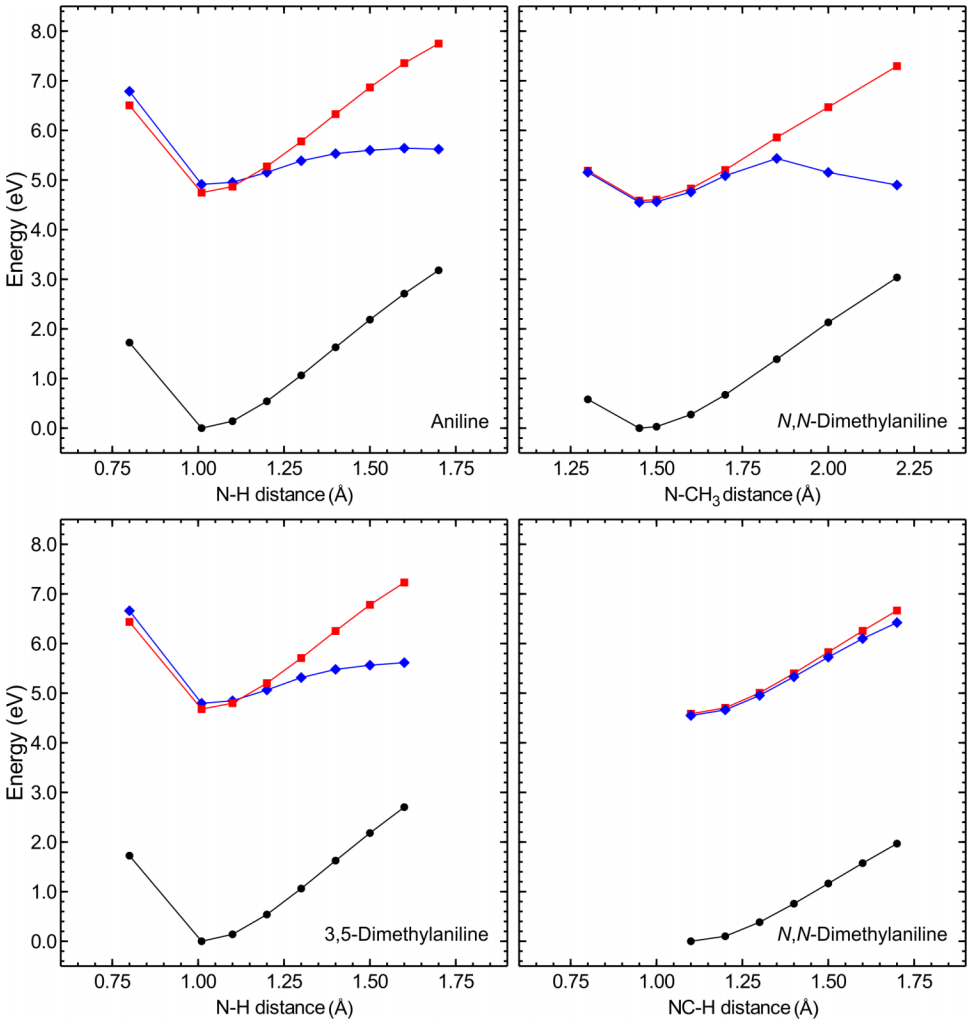

FIG. 8. EOM-CCSD/aug-cc-pVDZ potential energy cuts along the N–H stretching coordinate (aniline, 3,5-DMA) and the N–CH_3 and NC–H stretching coordinates (N,N-DMA) for the S_0 (●), $S_1(\pi\pi^*)$ (■), and $S_2(3s/\pi\sigma^*)$ (♦) states. For additional details, see the main text.

s-type Gaussian basis function with the smallest exponent in the aug-cc-pVDZ set, $\zeta = 0.061\ 24$). This drops by a factor of ~2.5 over the same region. This is consistent with a state-based picture from considering the EOM-CC amplitudes. The magnitude of the dominant excitation from a π orbital into $3s/\sigma^*$ clearly decreases as the bond is stretched, with other inter valence excitation amplitudes gaining in magnitude. Taken in combination, the data in Figs. 9(a) and 9(b) clearly reveal a significant reduction in the 3s Rydberg character contribution to the S_2 state overall (at the expense of more valence character) as the N–H bond is extended. This can be qualitatively seen by contrasting the $3s/\pi\sigma^*$ orbital at equilibrium (N–H = 1.01 Å) and at an extended distance (N–H = 1.7 Å), as shown in Fig. 9(c). At equilibrium, the orbital is almost entirely 3s Rydberg in character with a very small opposite phase amplitude contribution along the N–H bond. As the bond is extended, state mixing becomes stronger with the 3s coefficient dropping and (in this orientation) nitrogen p_y character mixing in, such that the inner valence p_y coefficient is −0.170 46 at 1.7 Å.

To further characterize the electronic states of aniline along the N–H stretching coordinate, we have performed LR-CCSD calculations to obtain excited state dipole moments (as orbital unrelaxed excited-state first-order properties).[42,43] For consistency, ground state CCSD dipole moments were also computed without orbital relaxation. We note that orbital relaxation has only small effect on the ground state dipole moments (1.457 D relaxed vs. 1.468 D unrelaxed at N–H = 1.01 Å). Changes in the overall dipole moment are plotted in Fig. 9(d). These property surfaces also indicate that valence character increases at the expense of 3s Rydberg character along the N–H stretching coordinate. While the ground state and ππ* dipole moments decrease only slightly, there is a significant reduction in the $3s/\pi\sigma^*$ state dipole, which changes from 7.911 D vertically excited (N–H = 1.01 Å), to 4.182 D at 1.7 Å. We note that the ππ* and $3s/\pi\sigma^*$ states cross around 1.2 Å and that at this geometry, all excited state properties are strongly mixed. This gives rise to the pronounced spikes in the otherwise smooth variation of the data. One of the strongest attributes of applying LR and EOM approaches to excited states is their correct and balanced description of such state mixing.[44] It is important to note that the $S_1(\pi\pi^*)/S_2(3s/\pi\sigma^*)$ interaction is only really important in a very narrow range of geometries where these states non-adiabatically couple. This means that for our results, only those shown at 1.2 Å have any degree of $S_1(\pi\pi^*)/S_2(3s/\pi\sigma^*)$ mixing while all others can be thought of as essentially diabatic state properties.

We have also computed excited-state second-moments of the electronic charge distribution. These $\langle\alpha\beta\rangle\ \{\alpha\beta \in x,y,z\}$ have been used as a main tool to investigate Rydberg character

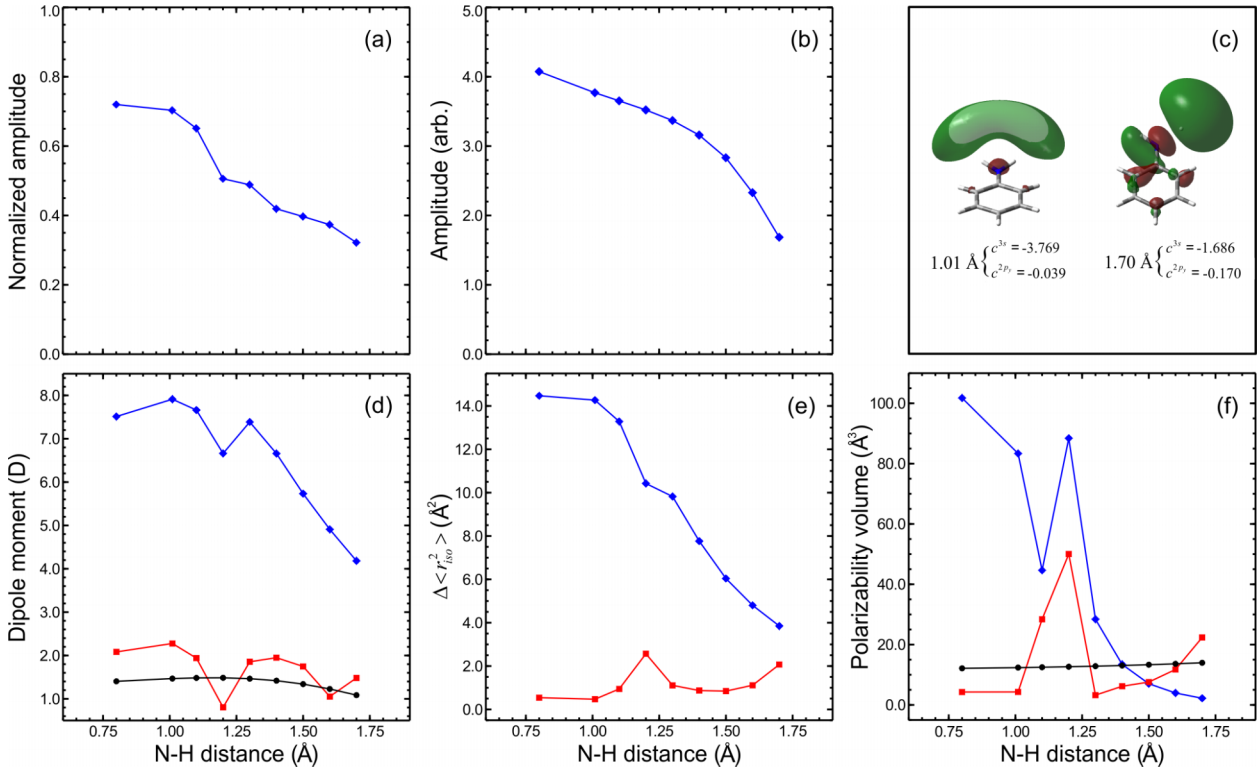

FIG. 9. Evolution of electronic state properties for the S_0 (•), $S_1(\pi\pi^*)$ (■), and $S_2(3s/\pi\sigma^*)$ (♦) states of aniline as a function of N-H bond extension. For further details, see main text. (a) Normalized EOM-CCSD right eigenvector amplitude for the $3s/\pi\sigma^*$ state, (b) un-normalized LCAO coefficient of the uncontracted nitrogen 3s basis function within the $3s/\pi\sigma^*$ state, (c) $3s/\pi\sigma^*$ orbital plot at 1.01 Å and 1.7 Å, (d) dipole moment, (e) isotropic invariant of the excited-state second-moment of the electronic charge distribution with respect to the ground state, and (f) isotropic polarizability volume.

in several pioneering studies (see, for example, Ref. 3). Of particular relevance to the parameterization of excited state, Rydberg character is the size of the isotropic invariant of the second-moment tensor relative to the S_0 ground state $\Delta\langle r_{iso}^2\rangle$. For each state, $\langle r_{iso}^2\rangle$ is obtained from the average of the trace of the second moment charge distribution tensor, i.e., $\langle r_{iso}^2\rangle = \frac{1}{3}(\langle x^2\rangle + \langle y^2\rangle + \langle z^2\rangle)$. As discussed by Reisler and Krylov,[3] valence states typically exhibit $\Delta\langle r_{iso}^2\rangle$ values close to 1 Å^2, whereas for 3s Rydberg states, this value may be in the region of 12 Å^2. The evolution of $\Delta\langle r_{iso}^2\rangle$ vs. N-H bond extension for the $S_1(\pi\pi^*)$ and $S_2(3s/\pi\sigma^*)$ states is shown in Fig. 9(e). In the former case, $\Delta\langle r_{iso}^2\rangle$ is small (~1 Å^2) at all geometries. In the latter instance, however, $\Delta\langle r_{iso}^2\rangle$ decreases considerably as the N–H bond is extended, falling from 14.470 Å^2 to 3.849 Å^2 over the range of distances sampled, once again illustrating the dramatic reduction in the Rydberg character of the $S_2(3s/\pi\sigma^*)$ state as the N–H bond extends.

Finally, the isotropic excited state polarizability volume ($\bar{\alpha}$) was also investigated. This is related to the trace of the polarizability tensor, in a similar manner to that of the second moment of charge tensor above, i.e., $\bar{\alpha} = \frac{1}{3}(\alpha_{xx} + \alpha_{yy} + \alpha_{zz})$. Other than the very strong state-mixing at around 1.2 Å, the $3s/\pi\sigma^*$ state polarizability volume decreases rapidly with increased N–H distance, starting from a considerably larger value that obtained for the $\pi\pi^*$ and S_0 states (see Fig. 9(f)). These trends are consistent with the other property surfaces and further validate the increasing valence and decreasing Rydberg character along this coordinate. As will be expanded upon further below, these significant changes in the $3s/\pi\sigma^*$ electronic state character as a function of bond extension have important implications for the interpretation of our experimental TRPEI data.

IV. DISCUSSION

A. τ_2 and τ_3 decay associated spectra

For all three molecules under study, the DAS plots presented in Fig. 6 are broadly similar both in terms of numerical time-constants and also the relative shapes and amplitudes of the spectral features. The only significant difference is the absence of any negative amplitude in the τ_1 DAS obtained for 3,5-DMA when compared to aniline and *N*,*N*-DMA (an issue, we will return to later). We also note that there are many similarities between the DAS plots in Fig. 6 and those we obtained previously for the case of aniline following excitation at 269.5 nm and 265.9 nm (populating the lowest lying vibrational levels supported by the shallow potential well along the $S_2(3s/\pi\sigma^*)$ N–H coordinate, in addition to the $S_1(\pi\pi^*)$ state).[1] In particular, the shapes and relative amplitudes of the τ_2 and τ_3 DAS are strikingly similar in all the data presented in this current study and our earlier work. As such, we interpret the τ_2 and τ_3 DAS in our new data for all three molecules as we did previously—a component of the initial excitation at 250 nm directly populates the $S_1(\pi\pi^*)$ state which then undergoes ultrafast intramolecular vibrational redistribution (IVR). This leads to changes in the Franck-Condon factors for ionization which manifest as a temporal evolution of the ionization cross section (0.5–2.2 ps, as modelled by τ_2). The $S_1(\pi\pi^*)$ state then

subsequently decays on a much longer time scale (~200 ps, as modelled by τ_3). Ultrafast (i.e., sub-picosecond) IVR has been previously reported in the $S_1(\pi\pi^*)$ state of chlorobenzene[45] and the ground state of benzene and the difluorobenzenes.[46] We have also previously attributed the same process to dynamical observations in the excited state dynamics of phenol and the dihydroxybenzenes.[24] In the experiments under discussion here, we are in excess of 6000 cm^{-1} above the $S_1(\pi\pi^*)$ origin in all cases, which is considerably higher than the experimentally determined IVR onset threshold in the excited $^1(\pi\pi^*)$ states of similar aromatic systems such as hydroquinone (1650 cm^{-1}) and anisole (940 cm^{-1}).[47,48] The ultimate fate of the $S_1(\pi\pi^*)$ state is not resolved in our measurements but several possibilities suggested on the basis of previous work in aniline include fluorescence,[49] intersystem crossing to lower-lying triplet states,[50] and internal conversion back to the S_0 ground state, where the role played by prefulvene-like structures has attracted some recent attention.[12,14] Theoretical work by Fielding and co-workers predicts aniline has four CIs connecting the $S_1(\pi\pi^*)$ and S_0 states, the lowest lying of which has a transition state located at ≥4.96 eV above the S_0 minimum energy.[14] The relatively long $S_1(\pi\pi^*)$ state lifetime seen in our data (180-230 ps) suggests, however, that this transition state is not directly accessible following excitation at 250 nm (also 4.96 eV) in any of the three systems under investigation.

B. τ_1 decay associated spectra

We now consider the extremely short-time (~100 fs) dynamics observed in our data, as described by the τ_1 DAS in Fig. 6. In all three molecules, there is a pronounced sharp peak (appearing between 0.9 eV and 1.2 eV, depending on the system) which has a relatively high anisotropy parameter β_2 associated with it (see Fig. 7). As confirmed theoretically in Sec. III, the $S_2(3s/\pi\sigma^*)$ state exhibits considerable 3s Rydberg character in the vertical Franck-Condon region. Single-photon ionization from an orbital possessing such character should therefore give rise to photoelectron partial waves of predominantly p character that peak strongly along the direction of laser polarization and exhibit a (relatively) large positive value for the β_2 anisotropy parameter. A strong propensity for diagonal ionization would also be expected, giving rise to a narrow peak in the photoelectron spectrum. The presence of the $S_2(3s/\pi\sigma^*)$ state is therefore clearly revealed in the data obtained for all three systems via the sharp feature in the 0.9-1.2 eV region of the τ_1 DAS. We note that the relative amplitude of this feature is considerably more intense than was the case in our previous aniline work following excitation at, or just above, the $S_2(3s/\pi\sigma^*)$ origin. In the earlier study, excitation was to single vibrational levels supported by the shallow potential well along the N–H stretching coordinate in the $S_2(3s/\pi\sigma^*)$ state. As such, only a fraction of the bandwidth associated with the broadband femtosecond pump pulse was resonant with this transition. In contrast, the full pump bandwidth was potentially able to initiate transitions to $S_1(\pi\pi^*)$ since the much higher density of associated vibrational states acts as an effective continuum. At 250 nm, transitions to the $S_2(3s/\pi\sigma^*)$ state also now sample a continuum as we are exciting to a purely repulsive part of the $S_2(3s/\pi\sigma^*)$ potential.

The sharp Rydberg feature in the τ_1 DAS is superimposed on a broader, short-lived background that exhibits a lower value of β_2. This extends from ~0.5 eV to between 1.3 and 1.7 eV, depending on the system. As already shown theoretically for the case of aniline, the 3s Rydberg character of the $S_2(3s/\pi\sigma^*)$ state decreases considerably when the N–H bond is extended. Critically, this evolution of the orbital character will occur extremely rapidly as the wavepacket initially prepared on the S_2 potential (which, at 250 nm, we assume to be purely repulsive) undergoes ballistic motion along the N–H coordinate. Given our experimental instrument response function of 130 fs, we are unable to resolve this evolution temporally—even upon replacing the N-H group with N–CH_3, as in the case of *N*,*N*-DMA. However, we suggest that our data appear to reflect this evolution in a *spectrally averaged* way as the increase in valence character of the S_2 state at extended N–H/N–CH_3 distances (at the expense of the Rydberg character) might well be expected to lead to a reduction in the propensity for diagonal ionisation (leading to a broader feature in the photoelectron spectra/τ_1 DAS) and also a reduction in the β_2 anisotropy parameter associated with this ionization signal—as appears to be observed. As seen in Fig. 6, the ionization signal originating from the valence character of the $S_2(3s/\pi\sigma^*)$ state extends to either side of the sharp Rydberg feature. This accounts for the small shoulder on the one-colour ionization data in Fig. 3 that is evident before the apparent onset threshold for excitation S_{3+} is reached energetically. Similar ideas relating to the observation of distinct ionization signatures originating from the Rydberg and valence components of the $S_2(3s/\pi\sigma^*)$ state in aniline have previously been discussed by Fielding and co-workers,[13,28] although their assignment and interpretation of such features are different to our own. More generally, the reduction in Rydberg character as a function of bond extension in mixed Rydberg/valance states may have important implications for time-resolved dynamical data in other systems: the presence of narrow spectral features with pronounced angular distributions clearly provides a strong and extremely useful $3s/\pi\sigma^*$ state indicator. However, this would seem to apply only in the vertical FC region (i.e., at short bond extensions), as evidenced here in the case of direct excitation to $S_2(3s/\pi\sigma^*)$ and indirectly in our previous work on phenol and the dihydroxybenzenes, where population is trapped at short distances in a potential well resulting from a coupling interaction between the (initially populated) $S_1(\pi\pi^*)$ and $S_2(3s/\pi\sigma^*)$ states.[24] In situations where a state of $3s/\pi\sigma^*$ character is only populated via internal conversion at more extended bond distances (i.e., far from the FC region), such distinct ionization signatures may not therefore be observed, possibly preventing unambiguous assignment and complicating any dynamical interpretation.

In the very low (<0.5 eV) kinetic energy region, the τ_1 DAS obtained for aniline and *N*,*N*-DMA shows negative amplitude, whereas in 3,5-DMA, this is not the case. As discussed earlier, negative amplitude features obtained from the global fitting procedure we have used are strongly indicative of sequential population transfer dynamics. In

aniline and *N*,*N*-DMA, the position of the negative amplitude feature overlaps well with the τ_2 and τ_3 DAS that we have assigned to the S_1 ($\pi\pi^*$) state. In agreement with Fielding and co-workers,[13] we therefore suggest this feature is a direct consequence of ultrafast $S_2(3s/\pi\sigma^*) \rightarrow S_1(\pi\pi^*)$ internal conversion occurring in ~100 fs. This is in contrast to our previous aniline work exciting at or just above the $S_2(3s/\pi\sigma^*)$ origin, where no clear evidence of such internal conversion was revealed and tunnelling under the barrier along the N–H stretching coordinate on the $S_2(3s/\pi\sigma^*)$ potential surface was invoked as the primary decay pathway.[1]

Although the relative amplitude of the negative feature in the τ_1 DAS is somewhat larger in *N*,*N*-DMA than in aniline, we are unable to definitively deduce the relative fraction of population transfer in the two systems as we do not know the relative absorption and ionization cross sections of the $S_1(\pi\pi^*)$ and $S_2(3s/\pi\sigma^*)$ states (and so are unable to determine their initial relative populations and any differences in sensitivity to probing them). On the other hand, the fact that the negative going signals do not exactly "mirror" the positive amplitudes in the τ_3 DAS means that we can at least be confident that both the $S_1(\pi\pi^*)$ and $S_2(3s/\pi\sigma^*)$ states are excited directly to some extent. Attempting to expand on this issue further, we are, however, able to make some (speculative) assumptions that enable us to try and comment on the relative contributions that various processes may make to the overall dynamics—particularly for the case of aniline, which has been far more extensively investigated than the two methyl-substituted systems. On the basis of our own calculations (see Table I), as well as those reported by others, the absorption cross section for single-photon excitation to the $S_2(3s/\pi\sigma^*)$ state in aniline is significantly smaller than that for $S_1(\pi\pi^*)$.[12,18] However, we suggest that the *photoionization cross section* for the $S_2(3s/\pi\sigma^*)$ state in aniline is much larger than for $S_1(\pi\pi^*)$. This is initially hinted at, for example, by recent work from Vallance and co-workers that establishes a strong positive linear correlation between static polarizability and absolute (ground state) electron impact ionization cross section.[51,52] For a wide range of small organic molecules, electronic polarizability volumes between 2 and 15.5 Å^3 gave corresponding maxima in the total ionization cross section of 2.5-23 Å^2. Similar correlations in relative ionization cross-section size were also seen to extend over a wider range of electron impact energies. To the best of our knowledge, the only investigation into the existence of a similar relationship in low-energy photoionization is that undertaken by Mullica and co-workers.[53] This work did not claim to establish a general correlation but did report clear trends in groups of chemically related systems. To begin exploring this idea again, we have compared the calculated polarizability volume data for 27 molecular systems reported by Vallance and co-workers with experimental photoionization cross-section information obtained from a number of sources.[54–62] The outcome of this (for a photon energy of 11.5 eV) is presented in Fig. 10. A clear positive relationship is revealed between the two quantities—as illustrated, for example, by the fact that a linear fit to the data yields a correlation coefficient of $r = 0.91$ (and a coefficient of determination $R^2 = 0.83$). However, more data (particularly for systems with polarizability volumes >15 Å^3)

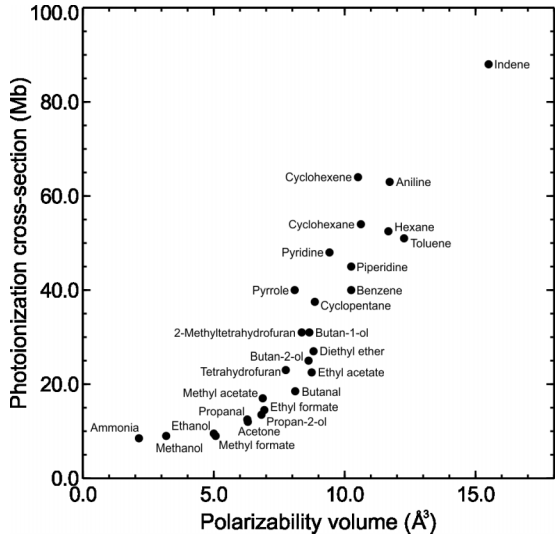

FIG. 10. Photoionization cross section (at a photon energy of 11.5 eV) plotted against polarizability volume for 27 small molecules. Polarizability data were taken from Refs. 51 and 52. Experimental cross-section data may be found in Refs. 54–62.

are required to confirm the exact nature of this relationship (linear or otherwise) over a wider range of values. Data for a larger number of chemically similar systems would also be desirable to investigate our initial findings in a more detailed and systematic manner. Nevertheless, Fig. 10 establishes a strong general trend relating increased polarizability volume to a larger (low-energy) photoionization cross section. This result is of key relevance, here, as our calculations (see Fig. 9(f)) predict an extremely large difference in the polarizability volumes for the $S_1(\pi\pi^*)$ and $S_2(3s/\pi\sigma^*)$ states in aniline—particularly at short N-H distances (e.g., 4.29 Å^3 vs. 83.37 Å^3, respectively, at the S_0 equilibrium geometry). Neglecting Franck-Condon and excited-state alignment effects, we therefore suggest that the $S_2(3s/\pi\sigma^*)$ ionization cross section may (conservatively) be at least an order of magnitude larger than for $S_1(\pi\pi^*)$—even if the correlation seen in Fig. 10 does not continue to extend in the same manner to higher values of the polarizability volume or follow quite the same trend for electronically excited states. Given the similar amplitude of the features attributable to the $S_1(\pi\pi^*)$ and $S_2(3s/\pi\sigma^*)$ states in our raw photoelectron and DAS data (see Figs. 5 and 6), we therefore conclude that the fraction of initial population prepared in $S_2(3s/\pi\sigma^*)$ is likely to be very small compared to $S_1(\pi\pi^*)$—i.e., it is a minor channel in the overall dynamics following 250 nm excitation. On the basis of the same argument, we also suggest that although our ionization-based experiment is very sensitive to population within $S_2(3s/\pi\sigma^*)$, sensitivity in tracking this population is reduced considerably once it transfers to $S_1(\pi\pi^*)$. As such, the relatively small negative amplitude in the aniline τ_1 DAS may, in fact, be reflecting a large fraction of population transfer from $S_2(3s/\pi\sigma^*)$. Although we have not evaluated polarizability volumes for *N*,*N*-DMA, a similar argument might also be expected to apply in this instance. Finally, here, we reiterate that, on the basis of our calculations in Sec. III, the efficiency of $S_2(3s/\pi\sigma^*)$ ionization in aniline (relative to the $S_1(\pi\pi^*)$ state) will also evolve rapidly as a function of N–H distance.

Although our own experiments are not able to directly resolve this, the averaging of such an effect clearly adds an additional layer of complexity to the detection sensitivity argument outlined above. Furthermore, it may also be a significant convoluting factor that requires more detailed consideration in any future dynamical lifetime measurements undertaken with a considerably shorter instrument response function.

C. Internal conversion vs. direct dissociation

Although the DAS obtained for aniline and *N*,*N*-DMA offers strong evidence of $S_2(3s/\pi\sigma^*) \rightarrow S_1(\pi\pi^*)$ internal conversion, this is not the only possible decay pathway for the $S_2(3s/\pi\sigma^*)$ state following 250 nm excitation. Our TRPEI measurement is effectively "blind" to this alternative (non-internal conversion) pathway, but it is apparent in the work of the Ashfold and Stavros groups who have both reported H atom release occurring on a very rapid time scale in aniline. This was inferred from photofragment recoil anisotropy and, in the latter case (a time-resolved photofragment imaging study), also from the appearance time (<1 ps) of the H atom photoproducts.[10,12] In both studies, the origin of this process was attributed to dissociation along the N–H coordinate of the $S_2(3s/\pi\sigma^*)$ state. Contrary to our own interpretation, however, these groups concluded that the $S_2(3s/\pi\sigma^*)$ state was populated following internal conversion from $S_1(\pi\pi^*)$. Given the long lifetime of the $S_1(\pi\pi^*)$ state relative to that of $S_2(3s/\pi\sigma^*)$, this pathway seems unlikely on the basis of simple kinetics-based arguments unless the system is only able to sample the $S_1(\pi\pi^*)/S_2(3s/\pi\sigma^*)$ CI for a limited time before the $S_1(\pi\pi^*)$ state relaxes—as previously noted by Longarte and co-workers.[11]

The possible existence of a second, alternative decay pathway for the $S_2(3s/\pi\sigma^*)$ state is also suggested by the fact that in 3,5-DMA, there is no negative amplitude in the τ_1 DAS providing any clear evidence of significant $S_2(3s/\pi\sigma^*) \rightarrow S_1(\pi\pi^*)$ internal conversion. However, population is still moving out of the $S_2(3s/\pi\sigma^*)$ state extremely rapidly, and so dissociation along the N–H stretching coordinate, therefore, also seems the most likely candidate for an alternative decay mechanism in this instance. It is interesting to compare the relative size of the broad positive amplitude feature in the τ_1 DAS (attributed to increasing $\pi\sigma^*$ character extended at N–H distances) with the sharp anisotropic peak at ~1.0 eV (attributed to dominant 3s Rydberg character at short N–H distances) seen in aniline and 3,5-DMA. In the former case, the broad feature is much less pronounced. Assuming that the evolution of $S_2(3s/\pi\sigma^*)$ sensitivity to ionization detection as a function of N–H extension is similar in these two systems (which is not unreasonable given the data presented in Table I and Fig. 8), we suggest that a much larger fraction of $S_2(3s/\pi\sigma^*)$ population in 3,5-DMA may be sampling more extended N–H distances (i.e., those beyond the crossing point with $S_1(\pi\pi^*)$ at ~1.2 Å)—indicating a greater propensity (when compared to aniline) for dissociation at the expense of internal conversion.

In *N*,*N*-DMA, the observation of a similar $S_2(3s/\pi\sigma^*)$ lifetime to that seen in the other two systems (≤100 fs) implies that any dissociation along the N–CH_3 stretching coordinate must be direct (rather than mediated via tunnelling) if it is to compete effectively with internal conversion. This appears to be confirmed by the fact that (i) excitation at 250 nm in aniline almost certainly excites above the $S_2(3s/\pi\sigma^*)$ N–H barrier[2] and (ii) our calculations predict a similar barrier height but a lower $S_2(3s/\pi\sigma^*)$ origin energy in *N*,*N*-DMA (see Fig. 8). As in aniline, we may therefore assume that both decay pathways are (in principle) active; although we are clearly unable to quantify the size of the contribution, each process makes to the overall $S_2(3s/\pi\sigma^*)$ relaxation in either molecule. In spite of this limitation, however, additional insights into the apparent differences in relative propensity for dissociation vs. internal conversion in all the three systems under investigation are revealed through analysis of the angular information provided by the photoelectron imaging approach.

D. Photoelectron angular distributions

Recent experimental and theoretical studies conducted on aniline have concluded that the critical internal molecular coordinates responsible for promoting non-adiabatic coupling between the $S_1(\pi\pi^*)$ and $S_2(3s/\pi\sigma^*)$ states are extension along the N–H bond and out-of-plane distortions of the aromatic ring system.[10,12] More generally, the same types of motions have been consistently implicated in mediating similar excited state interactions in a wide range of other aromatic systems including phenols, indoles, pyrroles, etc.[8,9] As argued previously by ourselves[24] and others,[63–65] non-adiabatic coupling interactions between different states effectively mixes their electronic (or vibronic) character and this may be reflected in the temporal evolution of the PADs observed in a TRPEI measurement. As is evident from Fig. 7, the three species under consideration undergo somewhat different temporal evolution of the β_2 anisotropy parameter. We suggest that this is directly related to the evolution of the $S_1(\pi\pi^*)$ electronic character that occurs upon each system sampling the correct molecular geometry to access the CI with the $S_2(3s/\pi\sigma^*)$ state. Critically, the observed relative time scales appear to be consistent with the assumption that extension along the N–H/N–CH_3 bond and out-of-plane distortions of the aromatic ring system is prerequisites for this interaction to occur. In aniline, there is no significant variation in β_2 with pump-probe delay, although it is clear from the DAS data presented in Fig. 6 that there is evidence of some non-adiabatic population transfer from $S_2(3s/\pi\sigma^*)$ to $S_1(\pi\pi^*)$—which must require some state mixing. We therefore assume that any such interaction is too fast to observe, given the temporal resolution of our experiment. As already discussed previously, we may also assume in aniline that both the internal conversion and direct dissociation pathways operate to some extent in the depletion of $S_2(3s/\pi\sigma^*)$ population—although we are unable to determine the relative contribution of each. Methylation of the N–H groups (*N*,*N*-DMA) slows down the $S_1(\pi\pi^*)/S_2(3s/\pi\sigma^*)$ interaction relative to aniline, but to a small extent as the motion along N–CH_3 coordinate is still very rapid (we assume any required motion associated with ring deformations remains unaffected). However, this effect is sufficient to permit the PAD evolution be revealed experimentally, with β_2 rising to a maximum value in 200 fs.

This time scale is still comparable to any direct dissociation and so internal conversion may compete to deplete population from $S_2(3s/\pi\sigma^*)$. Once again, the relative contributions of the two pathways cannot be quantified. Methylation of the ring system (3,5-DMA) has a more profound effect on the time scale for accessing the $S_1(\pi\pi^*)/S_2(3s/\pi\sigma^*)$ CI, presumably as a greater number of (more massive) atomic centres within the molecule need to be displaced. As seen in Fig. 7, β_2 now takes much longer (~1 ps) to rise to its maximum value. Since the direct $S_2(3s/\pi\sigma^*)$ dissociation pathway is not expected to slow down to the same extent, simple kinetics arguments therefore suggest the vast majority of population prepared initially in $S_2(3s/\pi\sigma^*)$ will now be depleted via direct dissociation before the system has a chance to access the $S_1(\pi\pi^*)/S_2(3s/\pi\sigma^*)$ CI. In contrast to aniline and *N*,*N*-DMA, no negative amplitude is therefore observed in the 3,5-DMA τ_1 DAS (see Fig. 6). Taken in combination, the observed energy-resolved (i.e., DAS) and angle-resolved data obtained for the three systems under study provide a clear and self-consistent picture of the dynamical process taking place following 250 nm excitation. Furthermore, our data provide an excellent demonstration of the interplay between structure and photochemical dynamics in the electronically excited states of molecules. This provides an important link to chemical function that is particularly relevant for a wide range of systems, including those mediating key processes in photobiology.

Finally, we briefly return to consider our previous measurements exciting aniline at or just above the $S_2(3s/\pi\sigma^*)$ origin (269.5 nm).[1] This earlier work did not observe any evolution of the β_2 anisotropy parameter as a function of pump-probe delay. At the time, this was taken as evidence that no $S_2(3s/\pi\sigma^*)/S_1(\pi\pi^*)$ interaction was occurring. However, this interpretation is potentially no longer fully reliable in light of the 250 nm data presented here, where we believe any changes in β_2 are too fast to resolve—especially given the somewhat longer instrument response used previously (180 fs vs. 130 fs currently). We stress that additional supporting evidence of no $S_2(3s/\pi\sigma^*)/S_1(\pi\pi^*)$ interaction also came from the absence of any negative amplitude in the τ_1 DAS—in contrast to the 250 nm case. As such, we believe our previously reported conclusions still hold. However, considering the arguments we have invoked regarding potential differences in the sensitivity of $S_2(3s/\pi\sigma^*)$ and $S_1(\pi\pi^*)$ to ionization detection, the reduced levels of relative initial $S_2(3s/\pi\sigma^*)$ population seen in our earlier work may mean that any small fraction internally converting to $S_1(\pi\pi^*)$ may not have been readily observed.

V. CONCLUSION

Time-resolved photoelectron imaging was used to investigate the potential role of non-adiabatic coupling between the $S_2(3s/\pi\sigma^*)$ and $S_1(\pi\pi^*)$ states in the electronic relaxation dynamics of aniline and two of its methyl-substituted derivatives following excitation at 250 nm. Analysis of the temporal evolution present in our photoelectron angular distribution data suggests that, in all cases, the coupling interaction is in operation at this specific excitation energy—although it is slowed down by an order of magnitude upon methylating the aromatic ring system at the 3 and 5 positions. Fits to our time-resolved photoelectron kinetic energy data appear to indicate that this coupling then provides a potential route for population transfer *from* the $S_2(3s/\pi\sigma^*)$ state *to* the $S_1(\pi\pi^*)$ state (both of which may be populated directly in the initial excitation). Additionally, the $S_2(3s/\pi\sigma^*)$ state may also potentially dissociate via a competing mechanism involving bond-fission along the N–H coordinate (or, in the case of *N*,*N*-DMA, the N–CH_3 coordinate). In aniline and *N*,*N*-DMA, we suggest both pathways may provide actively competing routes for population loss from the $S_2(3s/\pi\sigma^*)$ state. However, in 3,5-DMA, there is no evidence of any population transfer occurring via the $S_2(3s/\pi\sigma^*)/S_1(\pi\pi^*)$ internal conversion process. This may be rationalised in terms of simple kinetics since the relative rates of the two possible decay pathways are changed significantly upon methylation of the aromatic ring system, slowing the $S_2(3s/\pi\sigma^*)/S_1(\pi\pi^*)$ coupling interaction and effectively deactivating it as a decay pathway for the $S_2(3s/\pi\sigma^*)$ state. Our analysis was supported by a theoretical investigation of various excited state properties as a function of N–H bond extension in aniline. These calculations offer new insight into the evolution of the electronic character of the $S_2(3s/\pi\sigma^*)$ state. In particular, the 3s Rydberg contribution decreases significantly with increasing N–H bond length and this observation may be used to explain several features in our experimental data. More generally, we suggest that this observation is likely to be common to many other molecular species exhibiting excited states of mixed Rydberg/valence character. Our findings therefore have potentially important implications for the interpretation of dynamical data in all such systems. Finally, we have attempted to make some initial semi-quantitative arguments relating polarizability volumes to low-energy photoionization cross sections. This has implications for all experiments, where photoionization methods are used to investigate non-adiabatic dynamics evolving across different electronic states (with different associated detection sensitivities), potentially providing a useful aid in the interpretation and analysis of data obtained from a wide range of systems. However, more work is clearly required to fully quantify the general nature of any polarizability volume/photoionization cross-section relationship.

ACKNOWLEDGMENTS

This work was made possible by financial support from Engineering and Physical Sciences Research Council (EPSRC) Grant Nos. EP/G041717/1 and EP/K021052/1. M.J.P. is also supported by the European Research Council under the European Union's Seventh Framework Programme (FP7/2007-2013)/ERC Grant No. 258990. J.O.F.T. and S.W.C. thank Heriot-Watt University for Ph.D. funding. We also thank S. P. Neville and G. A. Worth (Birmingham) for helpful clarification on the nature of their EOM-CCSD calculations.

[1] J. O. F. Thompson, R. A. Livingstone, and D. Townsend, J. Chem. Phys. **139**, 034316 (2013).
[2] T. Ebata, C. Minejima, and N. Mikami, J. Phys. Chem. A **106**, 11070 (2002).
[3] H. Reisler and A. I. Krylov, Int. Rev. Phys. Chem. **28**, 267 (2009).
[4] C. S. Cockell and J. Knowland, Biol. Rev. **74**, 311 (1999).

[5]C. E. Crespo-Hernández, B. Cohen, P. M. Hare, and B. Kohler, Chem. Res. **104**, 1977 (2004).
[6]A. L. Sobolewski, W. Domcke, C. Dedonder-Lardeux, and C. Jouvet, Phys. Chem. Chem. Phys. **4**, 1093 (2002).
[7]I. Cnossen, J. Sanz-Forcada, F. Favata, O. Witasse, T. Zegers, and N. F. Arnold, J. Geophys. Res.: Planets **112**, E02008 (2007).
[8]M. N. R. Ashfold, G. A. King, D. Murdock, M. G. D. Nix, T. A. A. Oliver, and A. G. Sage, Phys. Chem. Chem. Phys. **12**, 1218 (2010).
[9]G. M. Roberts and V. G. Stavros, Chem. Sci. **5**, 1698 (2014).
[10]G. A. King, T. A. A. Oliver, and M. N. R. Ashfold, J. Chem. Phys. **132**, 214307 (2010).
[11]R. Montero, A. Peralta-Conde, V. Ovejas, R. Martínez, F. Castaño, and A. Longarte, J. Chem. Phys. **135**, 054308 (2011).
[12]G. M. Roberts, C. A. Williams, J. D. Young, S. Ullrich, M. J. Paterson, and V. G. Stavros, J. Am. Chem. Soc. **134**, 12578 (2012).
[13]R. Spesyvtsev, O. M. Kirkby, and H. H. Fielding, Faraday Discuss. **157**, 165 (2012).
[14]M. Sala, O. M. Kirkby, S. Guérin, and H. H. Fielding, Phys. Chem. Chem. Phys. **16**, 3122 (2014).
[15]K. Kimura, H. Tsubomura, and S. Nagakura, Bull. Chem. Soc. Jpn. **37**, 1336 (1964).
[16]L. Lagesson-Andrasko and V. Lagesson, *Handbook of Ultraviolet Spectra Vapour Phase 168-330 nm* (CG-UV Center, Linköping, Sweden, 2005).
[17]I. F. Galván, M. E. Martín, A. Muñoz-Losa, and M. A. Aguilar, J. Chem. Theory Comput. **5**, 341 (2009).
[18]Y. Honda, M. Hada, M. Ehara, and H. Nakatsuji, J. Chem. Phys. **117**, 2045 (2002).
[19]X.-J. Hou, P. Quan, T. Höltzl, T. Veszprémi, and M. T. Nguyen, J. Phys. Chem. A **109**, 10396 (2005).
[20]F. Wang, S. P. Neville, R. Wang, and G. A. Worth, J. Phys. Chem. A **117**, 7298 (2013).
[21]P. M. Wojciechowski, W. Zierkiewicz, D. Michalska, and P. Hobza, J. Chem. Phys. **118**, 10900 (2003).
[22]G. Raja, K. Saravanan, and S. Sivakumar, Elixir Comp. Chem. **44**, 7341 (2012).
[23]S. Zhang, B. Tang, Y. Wang, and B. Zhang, Chem. Phys. Lett. **397**, 495 (2004).
[24]R. A. Livingstone, J. O. F. Thompson, M. Iljina, R. J. Donaldson, B. J. Sussman, M. J. Paterson, and D. Townsend, J. Chem. Phys. **137**, 184304 (2012).
[25]U. Even, J. Jortner, D. Noy, N. Lavie, and C. Cossart-Magos, J. Chem. Phys. **112**, 8068 (2000).
[26]A. T. J. B. Eppink and D. H. Parker, Rev. Sci. Instrum. **68**, 3477 (1997).
[27]C. D. Cooper, A. D. Williamson, J. C. Miller, and R. N. Compton, J. Chem. Phys. **73**, 1527 (1980).
[28]R. Spesyvtsev, O. M. Kirkby, M. Vacher, and H. H. Fielding, Phys. Chem. Chem. Phys. **14**, 9942 (2012).
[29]M. A. Smith, J. W. Hager, and S. C. Wallace, J. Chem. Phys. **80**, 3097 (1984).
[30]J. W. Hager, M. A. Smith, and S. C. Wallace, J. Chem. Phys. **83**, 4820 (1985).
[31]V. K. Potapov and L. I. Iskakov, High Energy Chem. **5**, 264 (1971).
[32]J. P. Maier and D. W. Turner, J. Chem. Soc. Faraday Trans. **2**(69), 521 (1973).
[33]L. Szepes, G. Distefano, and S. Pignataro, Ann. Chim. **64**, 159 (1974).
[34]R. Montero, V. Ovejas, M. Fernández-Fernández, A. Peralta-Conde, and A. Longarte, J. Chem. Phys. **141**, 014303 (2014).
[35]O. Schalk, A. E. Boguslavskiy, and A. Stolow, J. Phys. Chem. A **114**, 4058 (2010).
[36]K. L. Reid, Annu. Rev. Phys. Chem. **54**, 397 (2003).
[37]T. Suzuki, Annu. Rev. Phys. Chem. **57**, 555 (2006).
[38]M. J. Frisch, G. W. Trucks, H. B. Schlegel, G. E. Scuseria, M. A. Robb, J. R. Cheeseman, G. Scalmani, V. Barone, B. Mennucci, G. A. Petersson, H. Nakatsuji, M. Caricato, X. Li, H. P. Hratchian, A. F. Izmaylov, J. Bloino, G. Zheng, J. L. Sonnenberg, M. Hada, M. Ehara, K. Toyota, R. Fukuda, J. Hasegawa, M. Ishida, T. Nakajima, Y. Honda, O. Kitao, H. Nakai, T. Vreven, J. A. Montgomery, Jr., J. E. Peralta, F. Ogliaro, M. Bearpark, J. J. Heyd, E. Brothers, K. N. Kudin, V. N. Staroverov, R. Kobayashi, J. Normand, K. Raghavachari, A. Rendell, J. C. Burant, S. S. Iyengar, J. Tomasi, M. Cossi, N. Rega, J. M. Millam, M. Klene, J. E. Knox, J. B. Cross, V. Bakken, C. Adamo, J. Jaramillo, R. Gomperts, R. E. Stratmann, O. Yazyev, A. J. Austin, R. Cammi, C. Pomelli, J. W. Ochterski, R. L. Martin, K. Morokuma, V. G. Zakrzewski, G. A. Voth, P. Salvador, J. J. Dannenberg, S. Dapprich, A. D. Daniels, Ö. Farkas, J. B. Foresman, J. V. Ortiz, J. Cioslowski, and D. J. Fox, GAUSSIAN 09, Revision D.01, Gaussian, Inc., Wallingford CT, 2009.
[39]K. Aidas, C. Angeli, K. L. Bak, V. Bakken, R. Bast, L. Boman, O. Christiansen, R. Cimiraglia, S. Coriani, P. Dahle, E. K. Dalskov, U. Ekström, T. Enevoldsen, J. J. Eriksen, P. Ettenhuber, B. Fernández, L. Ferrighi, H. Fliegl, L. Frediani, K. Hald, A. Halkier, C. Hättig, H. Heiberg, T. Helgaker, A. C. Hennum, H. Hettema, E. Hjertenæs, S. Høst, I.-M. Høyvik, M. F. Iozzi, B. Jansik, H. J. Aa. Jensen, D. Jonsson, P. Jørgensen, J. Kauczor, S. Kirpekar, T. Kjærgaard, W. Klopper, S. Knecht, R. Kobayashi, H. Koch, J. Kongsted, A. Krapp, K. Kristensen, A. Ligabue, O. B. Lutnæs, J. I. Melo, K. V. Mikkelsen, R. H. Myhre, C. Neiss, C. B. Nielsen, P. Norman, J. Olsen, J. M. H. Olsen, A. Osted, M. J. Packer, F. Pawlowski, T. B. Pedersen, P. F. Provasi, S. Reine, Z. Rinkevicius, T. A. Ruden, K. Ruud, V. Rybkin, P. Salek, C. C. M. Samson, A. S. d. Merás, T. Saue, S. P. A. Sauer, B. Schimmelpfennig, K. Sneskov, A. H. Steindal, K. O. Sylvester-Hvid, P. R. Taylor, A. M. Teale, E. I. Tellgren, D. P. Tew, A. J. Thorvaldsen, L. Thøgersen, O. Vahtras, M. A. Watson, D. J. D. Wilson, M. Ziolkowski, and H. Ågren, WIREs Comput. Mol. Sci. **4**, 269 (2014).
[40]Dalton, a molecular electronic structure program, Release DALTON2013.0 (2013), see http://daltonprogram.org.
[41]O. Christiansen, H. Koch, and P. Jørgensen, J. Chem. Phys. **105**, 1451 (1996).
[42]O. Christiansen, A. Halkier, H. Koch, P. Jørgensen, and T. Helgaker, J. Chem. Phys. **108**, 2801 (1998).
[43]O. Christiansen, P. Jørgensen, and C. Hättig, Int. J. Quantum Chem. **68**, 1 (1998).
[44]K. Sneskov and O. Christiansen, WIREs Comput. Mol. Sci. **2**, 566 (2012).
[45]Y.-Z. Liu, C.-C. Qin, S. Zhang, Y.-M. Wang, and B. Zhang, Acta Phys.-Chim. Sin. **27**, 965 (2011).
[46]R. S. von Benten, Y. Liu, and B. Abel, J. Chem. Phys. **133**, 134306 (2010).
[47]G. N. Patwari, S. Doraiswamy, and S. Wategaonkar, J. Phys. Chem. A **104**, 8466 (2000).
[48]R. Matsumoto, K. Sakeda, Y. Matsushita, T. Suzuki, and T. Ichimura, J. Mol. Struct. **735**, 153 (2005).
[49]R. Scheps, D. Florida, and S. A. Rice, J. Chem. Phys. **61**, 1730 (1974).
[50]B. Kim, C. P. Schick, and P. M. Weber, J. Chem. Phys. **103**, 6903 (1995).
[51]J. N. Bull, P. W. Harland, and C. Vallance, J. Phys. Chem. A **116**, 767 (2012).
[52]J. N. Bull, J. W. L. Lee, and C. Vallance, Phys. Chem. Chem. Phys. **16**, 10743 (2014).
[53]J. A. Beran, A. K. Dhingra, W.-S. Liu, and D. F. Mullica, Can. J. Chem. **53**, 1616 (1975).
[54]J. A. R. Samson, G. N. Haddad, and L. D. Kilcoyne, J. Chem. Phys. **87**, 6416 (1987).
[55]T. A. Cool, J. Wang, K. Nakajima, C. A. Taatjes, and A. McIlroy, Int. J. Mass Spectrom. **247**, 18 (2005).
[56]J. Wang, B. Yang, T. A. Cool, N. Hansen, and T. Kasper, Int. J. Mass Spectrom. **269**, 210 (2008).
[57]Z. Zhou, M. Xie, Z. Wang, and F. Qi, Rapid Commun. Mass Spectrom. **23**, 3994 (2009).
[58]M. Xie, Z. Zhou, Z. Wang, D. Chen, and F. Qi, Int. J. Mass Spectrom. **293**, 28 (2010).
[59]Z. Zhou, L. Zhang, M. Xie, Z. Wang, D. Chen, and F. Qi, Rapid Commun. Mass Spectrom. **24**, 1335 (2010).
[60]J. Wang, B. Yang, T. A. Cool, and N. Hansen, Int. J. Mass Spectrom. **292**, 14 (2010).
[61]M. Xie, Z. Zhou, Z. Wang, D. Chen, and F. Qi, Int. J. Mass Spectrom. **303**, 137 (2011).
[62]B. Yang, J. Wang, T. A. Cool, N. Hansen, S. Skeen, and D. L. Osborn, Int. J. Mass Spectrom. **309**, 118 (2012).
[63]C. Z. Bisgaard, O. J. Clarkin, G. Wu, A. M. D. Lee, O. Gessner, C. C. Hayden, and A. Stolow, Science **323**, 1464 (2009).
[64]Y.-I. Suzuki, T. Horio, T. Fuji, and T. Suzuki, J. Chem. Phys. **134**, 184313 (2011).
[65]G. Wu, P. Hockett, and A. Stolow, Phys. Chem. Chem. Phys. **13**, 18447 (2011).